Magnetic Resonance Imaging 63 (2019) 60–69

Contents lists available at ScienceDirect

Magnetic Resonance Imaging

journal homepage: www.elsevier.com/locate/mri

Original contribution

Evaluation of TP53/PIK3CA mutations using texture and morphology analysis on breast MRI

Woo Kyung Moon[a], Hong-Hao Chen[b], Sung Ui Shin[c], Wonshik Han[d], Ruey-Feng Chang[b,e,f,*]

[a] Department of Radiology, Seoul National University Hospital, South Korea
[b] Department of Computer Science and Information Engineering, National Taiwan University, Taipei, Taiwan
[c] Department of Radiology, Seoul National University Hospital Healthcare System Gangnam Center, South Korea
[d] Department of Surgery and Cancer Research Institute, Seoul National University College of Medicine, South Korea
[e] Graduate Institute of Biomedical Electronics and Bioinformatics, National Taiwan University, Taipei, Taiwan
[f] MOST Joint Research Center for AI Technology and All Vista Healthcare, Taipei, Taiwan

ARTICLE INFO

Keywords:
Breast Cancer
MRI
TP53
PIK3CA
Computer-aided diagnosis

ABSTRACT

Purpose: Somatic mutations in TP53 and PIK3CA genes, the two most frequent genetic alternations in breast cancer, are associated with prognosis and therapeutic response. This study predicted the presence of TP53 and PIK3CA mutations in breast cancer by using texture and morphology analyses on breast MRI.

Materials and methods: A total of 107 breast cancers (dataset A) from The Cancer Imaging Archive (TCIA) consisting of 40 TP53 mutation cancer and 67 cancers without TP53 mutation; 35 PIK3CA mutations cancer and 72 without PIK3CA mutation. 122 breast cancer (dataset B) from Seoul National University Hospital containing 54 TP53 mutation cancer and 68 without mutations were used in this study. At first, the tumor area was segmented by a region growing method. Subsequently, gray level co-occurrence matrix (GLCM) texture features were extracted after ranklet transform, and a series of features including compactness, margin, and ellipsoid fitting model were used to describe the morphological characteristics of tumors. Lastly, a logistic regression was used to identify the presence of TP53 and PIK3CA mutations. The classification performances were evaluated by accuracy, sensitivity, specificity, positive predictive value (PPV), and negative predictive value (NPV). Taking into account the trade-offs of sensitivity and specificity, the overall performances were evaluated by using receiver operating characteristic (ROC) curve analysis.

Results: The GLCM texture feature based on ranklet transform is more capable of recognizing TP53 and PIK3CA mutations than morphological feature, especially for the TP53 mutation that achieves statistically significant. The area under the ROC curve (AUC) for TP53 mutation dataset A and dataset B achieved 0.78 and 0.81 respectively. For PIK3CA mutation, the AUC of ranklet texture feature was 0.70.

Conclusion: Texture analysis of segmented tumor on breast MRI based on ranklet transform is potential in recognizing the presence of TP53 mutation and PIK3CA mutation.

1. Introduction

Somatic mutations in TP53 and PIK3CA genes are the two most frequent genetic alternations in breast cancer. The TP53 gene provides instructions for producing a tumor suppressor protein (p53) to preserve genome stability [1]. In human cells, both general metabolic activity and environmental factors can cause deoxyribonucleic acid (DNA) damage. The p53 proteins repair a damaged DNA by halting the cell cycle or induce apoptosis when the DNA cannot be repaired [2]. Therefore, the abnormal cells are avoided to be proliferated, and further prevents tumorigenesis. The p110α protein encoded by PIK3CA gene is responsible for performing the action of phosphatidylinositol 3-kinase (PI3K), which is also important for cell activities.

The most straightforward identification of gene mutations is to analyze the DNA sequence by molecular biological techniques, such as capillary electrophoresis [3] and denaturing high performance liquid chromatography (DHPLC) [4]. The other approaches observe the protein expression in tumor tissues through binding the specific antibodies and protein antigens in tissue section of tumor [5], including immunohistochemistry (IHC) [6] and enzyme-linked immunosorbent assay (ELISA) [7]. Both of them have its own weaknesses. DNA sequencing is time-consuming and cost ineffective [8], while the level of

* Corresponding author at: Department of Computer Science and Information Engineering, National Taiwan University, Taipei 106, Taiwan.
E-mail address: rfchang@csie.ntu.edu.tw (R.-F. Chang).

https://doi.org/10.1016/j.mri.2019.08.026
Received 24 August 2018; Received in revised form 27 June 2019; Accepted 15 August 2019

quantitative protein expression is limited by the sampled tissue, which cannot precisely represent the target protein in the overall tissue. On the contrary, determining the presence of gene mutation by image analysis provides a non-invasive and overall quantification. Moreover, it is convenient to repeat measurement, such as the evaluation of treatment response and regular follow-up care. Some literatures adopted non-invasive image texture analysis to predict gene mutations. For example, Dang et al. extracted MRI texture to predict p53 mutation of head and neck squamous cell carcinoma [9], Li et al. [10] predicted p53 status of lower-grade gliomas by texture and morphology analysis. Weiss et al. [11] analyzed lung CT texture to differentiate K-ras mutation from pan-wildtype tumors, Teo et al. [12] concluded that tumor morphological characteristics can facilitate the identification of PALB2 germline mutation.

In clinical pathology, protein p53 is regarded as a significant factor in triple-negative breast cancer which is commonly a mass with ill-defined or spiculated margin [13,14]. Additionally, TP53 mutations promote angiogenesis by regulating the angiogenic factor and vascular endothelial growth factor (VEGF) [15]. In terms of PIK3CA, protein p110α encoded by PIK3CA is multifactorial in tumor angiogenesis and regulation of proliferation [16]. Severe proliferation capacity is usually accompanied by angiogenesis and infiltration of surrounding tissues. The immature capillaries sprouting from the existing vessels infiltrated surrounding tissues and affect the intra-tumor texture and tumor morphology. Dynamic contrast-enhanced magnetic resonance imaging (DCE-MRI) is a highly sensitive tool for breast cancer diagnosis and the subtraction of pre-contrast image from post-contrast image facilitate to characterize tumor angiogenesis which supported neoplastic growth. Therefore, this study took advantage of the contrast enhancement of T1 weighted imaging to quantify the detail characteristics. Previous study [17,18] suggested that the proliferation activity and angiogenesis resulting tumor heterogeneity can be quantified by texture analysis. In this study, a gray level co-occurrence matrix (GLCM) texture [19] based on ranklet transform [20] and morphology analyses (compactness, margin, and ellipsoid fitting model) [21–24] were performed to predict the presence of TP53 mutation and PIK3CA mutation on breast MRI.

2. Materials

2.1. Data acquisition

There were two dataset used in this study to show the effect of difference somatic mutation identification approaches, whole-genome/whole-exome sequencing and IHC. Dataset A includes 139 breast MRI examinations in The Cancer Imaging Archive (TCIA) [25,26] at the time of this study, provided by Mayo Clinic, University of Pittsburgh Medical Center, Roswell Park Cancer Institute, University of Miami Miller School of Medicine, Memorial Sloan-Kettering Cancer Center, University of North Carolina, and University of Chicago. Dataset B contains 144 breast MRI examinations from Seoul National University Hospital with only TP53 genetic test results. Among these cases, 16 cases in dataset A and 22 cases in dataset B were excluded due to poor image quality judged by an experienced radiologist. In addition, to reduce the variation of the images in dataset A, one case scanned by a 3 Tesla of magnetic field strength and 15 cases acquired by Philips (Philips Medical Systems, Best, The Netherlands) scanner were excluded. As shown in Table 1, the resulting 107 breast masses (patient age range: 29–82 years; mean ± standard deviation (SD), 53.74 ± 11.14 years, tumor size range: 0.77–8.32 cm; mean: 2.24 cm) in dataset A and 122 breast mass (patient age range: 29–80 years; mean ± standard deviation (SD): 49.89 ± 10.12 years, tumor size range: 0.50–6.50 cm; mean: 2.52 cm) in dataset B proved by histological examination were used in this study. Dataset A comprised 40 TP53 gene mutation cancers and 67 without TP53 gene mutation; 35 PIK3CA gene mutation cancers and 72 without PIK3CA gene mutation by whole-genome or whole-exome sequencing. Dataset B contained 54 TP53 mutation cases and 68 without mutations by IHC.

Table 1
Characteristics of collected cases.

Parameters	Dataset A	Dataset B
Number of cases		
Total	107	122
TP53 mutation	40	54
Non-TP53 mutation	67	68
PIK3CA mutation	35	–
Non-PIK3CA mutation	72	–
Age (year)		
Mean ± SD	53.74 ± 11.14	49.89 ± 10.12
Range	29–82	29–80
Tumor size (cm)		
Mean	2.24	2.52
Range	0.77–8.32	0.50–6.50

3. Methods

The proposed scheme segmented the tumor area from the three-dimensional (3-D) breast MRI volume by a region growing technique [27]. Subsequently, 3-D ranklet transform was implemented on the subtraction image to obtain the ranklet coefficients of three directions (vertical, horizontal, and diagonal) for texture analysis. The GLCM texture features and morphological features (Table 2) were extracted. Lastly, a logistic regression [28] classifier was applied to recognize the presence of TP53 mutation and PIK3CA mutation. Fig. 1 shows the flowchart of the classification system.

3.1. Tumor segmentation

A medical contrast agent is commonly used to enhance vascular

Table 2
Definition of the 3-D texture and morphological features.

Category	Symbol	Description
Texture	$m(Energy_{orientation})$	Mean of energy
	$m(Entropy_{orientation})$	Mean of entropy
	$m(Correlation_{orientation})$	Mean of correlation
	$m(IDM_{orientation})$	Mean of inverse difference moment
	$m(Inertia_{orientation})$	Mean of inertia
	$m(CS_{orientation})$	Mean of cluster shade
	$m(CP_{orientation})$	Mean of cluster prominence
	$m(HC_{orientation})$	Mean of Haralick's correlation
	$\sigma(Energy_{orientation})$	Standard deviation of energy
	$\sigma(Entropy_{orientation})$	Standard deviation of entropy
	$\sigma(Correlation_{orientation})$	Standard deviation of correlation
	$\sigma(IDM_{orientation})$	Standard deviation of inverse difference moment
	$\sigma(Inertia_{orientation})$	Standard deviation of inertia
	$\sigma(CS_{orientation})$	Standard deviation of cluster shade
	$\sigma(CP_{orientation})$	Standard deviation of cluster prominence
	$\sigma(HC_{orientation})$	Standard deviation of Haralick's correlation
Morphology	C_1	Classical compactness
	C_2	New compactness
	R	Radius
	R_S	Spiculation
	ER_{axis}	Axis ratio
	$ER_{surface}$	Surface area ratio of tumor and ellipsoid
	ER_{and}	Volume coverage ratio
	EN_{in}	Number of inside regions
	EN_{out}	Number of outside regions
	EN_{io}	Sum of EN_{in} and EN_{out}
	EN_{a_in}	Number of inside angular regions
	EN_{a_out}	Number of outside angularregions
	EN_{a_io}	Sum of EN_{a_in} and EN_{a_out}
	E_{angle}	Orientation of ellipsoid

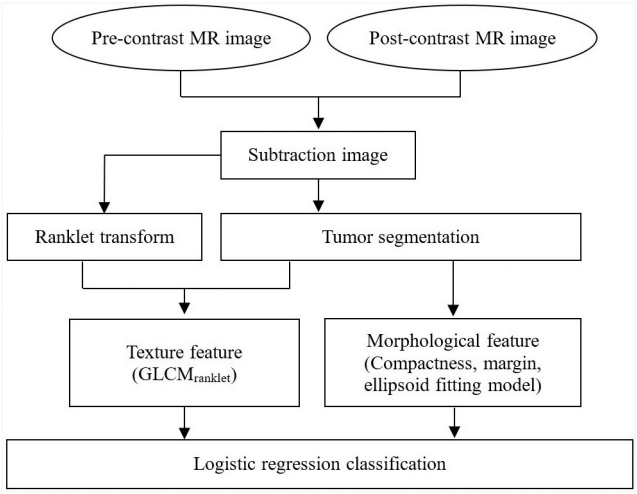

Fig. 1. Flowchart of the proposed scheme.

visibility. With the tumor growth, angiogenesis is a physiological process to supply nutrients and oxygen by formation of new vessels [29]. After contrast agent injection, water around the unpaired electrons of the contrast agent relaxes quickly. Hence the contrast between tumor and surrounding tissues of MR images is enhanced [30]. In this study, a subtraction image was calculated by subtracting the pre-contrast scan from the first post-contrast scan to obtain the clear tumor area. An edge-preserving smoothing technique, curvature anisotropic diffusion [31], was performed on the subtraction image to remove noise and retain the tumor boundary simultaneously. Afterwards, the tumor area was segmented by using a confidence connected technique [32] with a user-specified seed and a rectangular volume of interest (VOI) bounding the tumor. (see details in Section S1 of Supplemental Materials).

In order to eliminate cavities in tumor region, an iterative hole-filling filter [33] was applied to the region growing result. Pixels switch from background to foreground if its neighboring pixels are mostly foreground [17]. Fig. 2 shows an example of the tumor segmentation result.

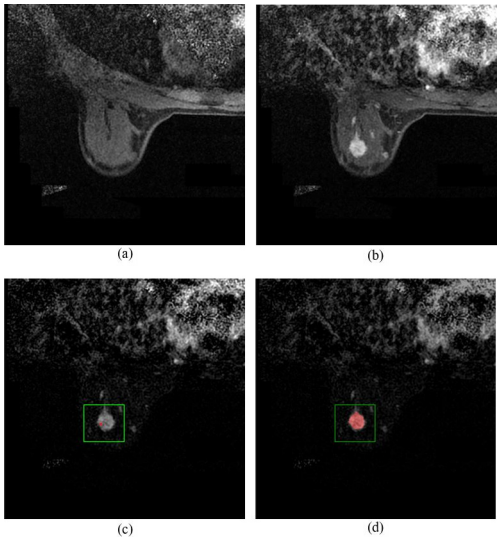

Fig. 2. Tumor segmentation result. (a) a pre-contrast slice; (b) a post-contrast slice; (c) the subtraction image with a user specified seed and VOI; (d) a slice of segmentation result.

3.2. Ranklet transform

Since the MRI studies of TCIA collected from multiple institutions are extremely heterogeneous in acquisition protocols and parameters. Texture analysis of MR images is influenced by image contrast which mainly defined by repetition time (TR) and spin echo time (TE) [34]. A image processing technique, ranklet transform [20], was performed on MR images before extracting texture feature. Ranklet transform [20] represents pixels in a relative order instead of their intensities with different orientations, containing vertical, horizontal, and diagonal. The property of relative order presentation contributes to overcome the contrast variations among MRI studies. Fig. 3 shows an example of ranklet transform results of different contrast adjustment methods, histogram equalization [35] and gamma correction [36]. The ranklet transform results of different contrast adjustment methods are almost identical.

3.3. GLCM texture feature

GLCM [19] is the most commonly used texture analysis technique which defines the occurrences of pixel pairs with specific values and spatial relationship in an image. In order to obtain clear intra-tumor structure, each intensity value in the subtraction image was performed a linearly transform [37,38] to normalize the intensities range from 0 to 255 (see details in Section *S2* in Supplemental Materials). Subsequently, the means and standard deviations of statistical measures including energy, entropy, correlation, inverse difference moment, inertia, cluster shade, cluster prominence, and Haralick's correlation of 13 directions were extracted respectively in the 3-D space.

3.4. Morphological feature

Morphological feature measured based on the contour of tumor region interprets the quantification of shape complexities. In breast tumor analysis, prior studies [17,39,40] exploit morphological feature to differentiate between benign and malignant, quantify tumor heterogeneity, and correlate with tumor subtypes. To investigate the morphological variations of TP53 mutation and PIK3CA mutation, this study extracted morphological features of compactness, margin, and ellipsoid fitting model from each tumor. Two kinds of compactness [22] were used to represent the degree to which a shape is compact. Radius (R) and spiculation (Rs) [21] depicted the tumor margin were also included. Furthermore, the ellipsoid fitting model [23,24] was applied to construct an ellipsoid model to fit the tumor under the condition of minimizing the distance between the ellipsoid and the tumor (Fig. 4). A total of 10 features of ellipsoid fitting model were extracted to measure the relation between the tumor and ellipsoid (see details in Section *S3* in Supplemental Materials).

4. Statistical analysis

To determine the normality of each feature, the Kolmogorov-Smirnov test [28] was applied to exam the distribution of each feature by comparing with a standard normal distribution. If a feature is normal distribution, the mean and standard deviation were given and the Student's t-test [28] was used to determine whether two sets of data are significantly different from each other. On the contrary, if a feature is not normal distribution, the median was given and the Mann-Whitney U test [28] was used. A logistic regression model and backward feature selection [41] were used to classify the presence of TP53 mutation and PIK3CA mutation. The training set and testing set were defined by using leave-one-out cross validation [42], whose model-building process was enclosed within the cross-validation loop, and the left-out sample was used as the testing sample. The cross-validation process is then repeated N times (N denotes the number of samples), with each of the left-out sample used exactly once as the validation data. In performance

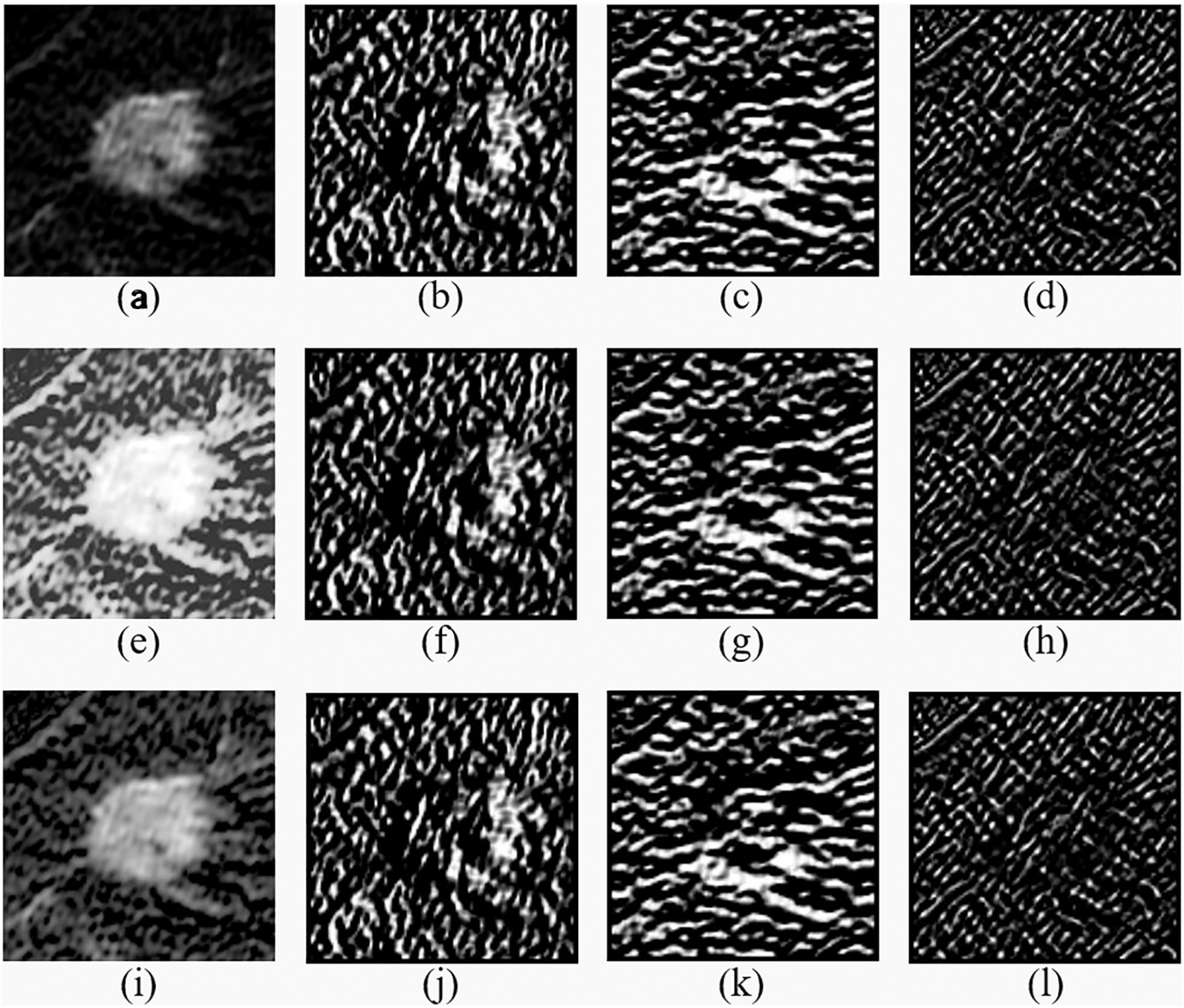

Fig. 3. Ranklet transform results of different contrast adjustment methods. (a), (e), and (i) are the original image, histogram equalization result, and gamma correction result ($\gamma = 0.5$). (b)–(d), (f)–(h), and (j)–(l) are the corresponding ranklet transform results with vertical, horizontal, and diagonal orientations.

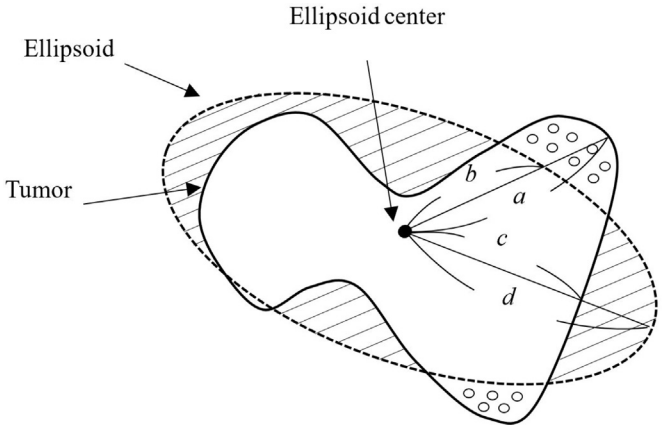

Fig. 4. An example of ellipsoid fitting model. The circled areas are outside regions and the slashed areas are inside regions. The angular degree of the outside region and inside region are a/b and c/d respectively.

comparison, the chi-square test [28] was applied to determine whether there is a significant difference between different feature sets. Additionally, considering the trade-offs between sensitivity and specificity, the receiver operating characteristic (ROC) curve analysis (the software package ROCKIT by professor C. E. Metz, University of Chicago, IL) was used to reveal the overall performance of each feature set. The z-test was also applied to determine the statistical significance between the area under the ROC curves (AUC). The Bonferroni–Holm correction [43] was adopted to adjust the p-values in performance comparison between different feature.

5. Results

The effect of each single texture feature on identifying TP53/PIK3CA mutations was also evaluated. Energy and inverse difference moment (IDM) represent the homogeneity of tumor area, entropy qualifies the randomness, correlation and Haralick's correlation measure of how correlated a pixel is to its neighbors over the tumor area, inertia implies contrast, cluster shade and cluster prominence characterizes the tendency of clustering of the pixels in the tumor area.

Table 3
Mean, SD, median, and *p*-values (Student's *t*-test or Manny-Whitney *U* test) of $GLCM_{ranklet}$ features in differentiating TP53 mutation (Dataset A).

Feature	Without TP53 Mutation		With TP53 Mutation		*p*-value
	Mean ± SD	Median	Mean ± SD	Median	
$m(Energy_{horizontal})$		8×10^{-4}		5×10^{-4}	0.009*
$m(Entropy_{horizontal})$		10.631		9.9926	0.145
$m(Correlation_{horizontal})$		2×10^{-4}		3×10^{-4}	0.006*
$m(IDM_{horizontal})$		0.055		0.054	0.534
$m(Inertia_{horizontal})$	2116.426 ± 934.203		1658.156 ± 749.632		0.006*
$m(CS_{horizontal})$	$-2.543 \times 10^{5} \pm 3.975 \times 10^{5}$		$-1.113 \times 10^{5} \pm 4.129 \times 10^{5}$		0.079
$m(CP_{horizontal})$	$3.173 \times 10^{8} \pm 1.625 \times 10^{8}$		$2.324 \times 10^{8} \pm 1.442 \times 10^{8}$		0.008*
$m(HC_{horizontal})$	$7.081 \times 10^{8} \pm 3.982 \times 10^{8}$		$6.764 \times 10^{8} \pm 2.840 \times 10^{8}$		0.660
$\sigma(Energy_{horizontal})$		2×10^{-4}		2×10^{-4}	0.052
$\sigma(Entropy_{horizontal})$		0.138		0.210	0.150
$\sigma(Correlation_{horizontal})$		4×10^{-5}		5×10^{-5}	0.020*
$\sigma(IDM_{horizontal})$		0.020		0.019	0.308
$\sigma(Inertia_{horizontal})$	810.929 ± 401.463		632.383 ± 270.169		0.014*
$\sigma(CS_{horizontal})$	$6.853 \times 10^{4} \pm 3.912 \times 10^{4}$		$6.244 \times 10^{4} \pm 4.064 \times 10^{4}$		0.444
$\sigma(CP_{horizontal})$	$4.686 \times 10^{7} \pm 2.207 \times 10^{7}$		$3.944 \times 10^{7} \pm 1.883 \times 10^{7}$		0.079
$\sigma(HC_{horizontal})$		2.052×10^{7}		21,482,530	0.982
$m(Energy_{vertical})$		8×10^{-4}		5×10^{-4}	0.031*
$m(Entropy_{vertical})$		10.544		10.077	0.097
$m(Correlation_{vertical})$		3×10^{-4}		2×10^{-4}	0.620
$m(IDM_{vertical})$		0.057		0.053	0.207
$m(Inertia_{vertical})$	1576.695 ± 689.924		1644.358 ± 695.592		0.626
$m(CS_{vertical})$		2216.9462		1046.9258	0.600
$m(CP_{vertical})$	$2.454 \times 10^{8} \pm 1.540 \times 10^{8}$		$2.319 \times 10^{8} \pm 1.259 \times 10^{8}$		0.638
$m(HC_{vertical})$		5.655×10^{8}		6.966×10^{8}	0.192
$\sigma(Energy_{vertical})$		2×10^{-4}		1×10^{-4}	0.237
$\sigma(Entropy_{vertical})$		0.123		0.260	0.068
$\sigma(Correlation_{vertical})$		4×10^{-5}		4×10^{-5}	0.695
$\sigma(IDM_{vertical})$		0.019		0.017	0.042*
$\sigma(Inertia_{vertical})$	593.306 ± 254.475		604.692 ± 254.542		0.823
$\sigma(CS_{vertical})$		3.822×10^{4}		3.964×10^{4}	0.497
$\sigma(CP_{vertical})$	$3.608 \times 10^{7} \pm 1.884 \times 10^{7}$		$3.449 \times 10^{7} \pm 1.767 \times 10^{7}$		0.667
$\sigma(HC_{vertical})$		2.317×10^{7}		2.030×10^{7}	0.061
$m(Energy_{diagonal})$		8×10^{-4}		5×10^{-4}	0.024*
$m(Entropy_{diagonal})$	10.337 ± 1.043		9.924 ± 1.184		0.062
$m(Correlation_{diagonal})$		3×10^{-4}		2×10^{-4}	0.226
$m(IDM_{diagonal})$		0.042		0.039	0.154
$m(Inertia_{diagonal})$	1854.058 ± 556.108		1973.570 ± 583.783		0.294
$m(CS_{diagonal})$		−3761.460		−4119.654	0.669
$m(CP_{diagonal})$	$7.748 \times 10^{7} \pm 4.335 \times 10^{7}$		$8.350 \times 10^{7} \pm 4.137 \times 10^{7}$		0.481
$m(HC_{diagonal})$	$3.342 \times 10^{8} \pm 1.595 \times 10^{8}$		$3.566 \times 10^{8} \pm 1.502 \times 10^{8}$		0.475
$\sigma(Energy_{diagonal})$		8×10^{-5}		7×10^{-5}	0.212
$\sigma(Entropy_{diagonal})$		0.115		0.155	0.103
$\sigma(Correlation_{diagonal})$		1×10^{-4}		1×10^{-4}	0.314
$\sigma(IDM_{diagonal})$		0.011		0.010	0.032*
$\sigma(Inertia_{diagonal})$	543.626 ± 183.477		560.450 ± 153.231		0.627
$\sigma(CS_{diagonal})$		1.985×10^{4}		1.857×10^{4}	0.716
$\sigma(CP_{diagonal})$	$1.765 \times 10^{7} \pm 9.244 \times 10^{6}$		$1.846 \times 10^{7} \pm 7.830 \times 10^{6}$		0.640
$\sigma(HC_{diagonal})$		1.013×10^{7}		9.703×10^{6}	0.518

* *p*-value < 0. × significance.

Table 3 lists all ranklet texture features for identifying TP53 mutation. In horizontal ranklet coefficients, the six features $m(Energy_{horizontal})$, $m(Correlation_{horizontal})$, $m(Inertia_{horizontal})$, $m(CP_{horizontal})$, $\sigma(Correlation_{horizontal})$, and $\sigma(Inertia_{horizontal})$ showed significant difference between tumors with normal TP53 and mutated TP53 gene. In vertical and diagonal ranklet coefficients, the mean energy and the standard deviation of inverse difference moment also achieve statistically significant. Noteworthy, the TP53 mutated cancers showed significantly smaller mean energy of ranklet coefficients in all orientation (horizontal, vertical, and diagonal) which imply that the TP53 mutated cancers are less textural uniform compared to the cancers without TP53 mutation. Table 4 displays that cancers with PIK3CA mutation had significant lower standard deviation of inertia in vertical orientation. But no morphological features were statistically significant in TP53 and PIK3CA mutation (see details in Section S4 in Supplemental Materials).

Fig. 5 displays a tumor of a 63-year-old woman. The tumor is textural uniform in the subtraction image and ranklet transform results, and was classified as normal TP53 tumor. Fig. 6 displays a tumor of a 75-year-old women. Compare to the normal TP53 case (Fig. 5), the tumor in Fig. 6 is less textural uniform in visual. The mean energy of ranklet transform coefficients are 0.00027, 0.00024, and 0.0004 for horizontal, vertical, and diagonal orientations which are < 0.00287, 0.00295, and 0.00301 of Fig. 5.

The comparison of classification performance of TP53/PIK3CA mutations of dataset A and dataset B by using $GLCM_{ranklet}$ texture feature and morphological feature are listed in Table 5 and 6. A cut of value was determined to select the higher sensitivity under the premise of maximizing accuracy. For TP53 mutation, the accuracy, sensitivity, specificity, positive predictive value (PPV), and negative predictive value (NPV) of $GLCM_{ranklet}$ feature are outperform than those of morphological feature in both dataset A (Table 5) and dataset B (Table 6) whether the reference standards were identified by whole-genome/whole-exome sequencing or IHC.

In terms of PIK3CA mutation, the accuracy, sensitivity, specificity, PPV, and NPV of $GLCM_{ranklet}$ feature also achieve higher values than those of morphological feature (Table 5). Taking into account the trade-

Table 4
Mean, SD, median, and *p*-values (Student's *t*-test or Manny-Whitney *U* test) of $GLCM_{ranklet}$ feature in differentiating PIK3CA mutation (dataset A).

Feature	Without PIK3CA Mutation		With PIK3CA Mutation		*p*-value
	Mean ± SD	Median	Mean ± SD	Median	
$m(Energy_{horizontal})$		6.85×10^{-4}		6.4×10^{-4}	0.900
$m(Entropy_{horizontal})$		10.340		10.799	0.575
$m(Correlation_{horizontal})$		2.35×10^{4}		2.1×10^{4}	0.465
$m(IDM_{horizontal})$		0.053		0.055	0.842
$m(Inertia_{horizontal})$	1919.639 ± 931.906		1997.507 ± 822.013		0.675
$m(CS_{horizontal})$	$-1.778 \times 10^{5} \pm 4.141 \times 10^{5}$		$-2.483 \times 10^{5} \pm 3.948 \times 10^{5}$		0.404
$m(CP_{horizontal})$	$2.761 \times 10^{8} \pm 1.613 \times 10^{8}$		$3.051 \times 10^{8} \pm 1.598 \times 10^{8}$		0.385
$m(HC_{horizontal})$	$7.023 \times 10^{8} \pm 4.051 \times 10^{8}$		$6.837 \times 10^{8} \pm 2.410 \times 10^{8}$		0.802
$\sigma(Energy_{horizontal})$		1.7×10^{-4}		1.7×10^{-4}	0.857
$\sigma(Entropy_{horizontal})$		0.144		0.143	0.678
$\sigma(Correlation_{horizontal})$		4×10^{-5}		4×10^{-5}	0.090
$\sigma(IDM_{horizontal})$		0.020		0.019	0.256
$\sigma(Inertia_{horizontal})$	747.147 ± 398.146		738.085 ± 298.310		0.905
$\sigma(CS_{horizontal})$	$6.511 \times 10^{4} \pm 4.068 \times 10^{4}$		$6.862 \times 10^{4} \pm 3.778 \times 10^{4}$		0.669
$\sigma(CP_{horizontal})$	$4.428 \times 10^{7} \pm 2.193 \times 10^{7}$		$4.367 \times 10^{7} \pm 1.970 \times 10^{7}$		0.888
$\sigma(HC_{horizontal})$		2.071×10^{7}		2.097×10^{7}	0.783
$m(Energy_{vertical})$		6.45×10^{-4}		5.3×10^{-4}	0.976
$m(Entropy_{vertical})$		10.373		10.624	0.717
$m(Correlation_{vertical})$		2.35×10^{-4}		3.2×10^{-4}	0.100
$m(IDM_{vertical})$		0.054		0.053	0.383
$m(Inertia_{vertical})$	1688.233 ± 660.136		1424.575 ± 724.018		0.063
$m(CS_{vertical})$		-5.45×10^{4}		4.144×10^{4}	0.181
$m(CP_{vertical})$	$2.482 \times 10^{8} \pm 1.399 \times 10^{8}$		$2.243 \times 10^{8} \pm 1.519 \times 10^{8}$		0.422
$m(HC_{vertical})$		6.126×10^{8}		5.730×10^{8}	0.793
$\sigma(Energy_{vertical})$		1.7×10^{-4}		1.2×10^{-4}	0.871
$\sigma(Entropy_{vertical})$		0.138		0.148	0.517
$\sigma(Correlation_{vertical})$		4×10^{-5}		4×10^{-5}	0.920
$\sigma(IDM_{vertical})$		0.018		0.019	0.383
$\sigma(Inertia_{vertical})$	632.275 ± 254.863		526.154 ± 238.074		0.042*
$\sigma(CS_{vertical})$		4.480×10^{4}		3.186×10^{4}	0.070
$\sigma(CP_{vertical})$	$3.787 \times 10^{7} \pm 1.863 \times 10^{7}$		$3.057 \times 10^{7} \pm 1.693 \times 10^{7}$		0.053
$\sigma(HC_{vertical})$		21,309,218		20,352,508	0.850
$m(Energy_{diagonal})$		6.45×10^{-4}		6.8×10^{-4}	0.604
$m(Entropy_{diagonal})$	10.137 ± 1.138		10.276 ± 1.063		0.548
$m(Correlation_{diagonal})$		2.5×10^{-4}		2.7×10^{-4}	0.215
$m(IDM_{diagonal})$		0.040		0.042	0.455
$m(Inertia_{diagonal})$	1954.156 ± 537.172		1784.727 ± 615.882		0.148
$m(CS_{diagonal})$		-1143.325		-4167.700	0.467
$m(CP_{diagonal})$	$8.145 \times 10^{7} \pm 4.173 \times 10^{7}$		$7.618 \times 10^{7} \pm 4.452 \times 10^{7}$		0.550
$m(HC_{diagonal})$	$3.458 \times 10^{8} \pm 1.643 \times 10^{8}$		$3.360 \times 10^{8} \pm 1.386 \times 10^{8}$		0.762
$\sigma(Energy_{diagonal})$		7×10^{-5}		8×10^{-5}	0.886
$\sigma(Entropy_{diagonal})$		0.119		0.120	0.803
$\sigma(Correlation_{diagonal})$		1×10^{-4}		1×10^{-4}	0.341
$\sigma(IDM_{diagonal})$		0.011		0.010	0.593
$\sigma(Inertia_{diagonal})$	559.278 ± 161.906		530.656 ± 192.825		0.423
$\sigma(CS_{diagonal})$		2.026×10^{4}		1.609×10^{4}	0.354
$\sigma(CP_{diagonal})$	$1.838 \times 10^{7} \pm 8.208 \times 10^{6}$		$1.708 \times 10^{7} \pm 9.737 \times 10^{6}$		0.471
$\sigma(HC_{diagonal})$		1.019×10^{7}		$9.549\,m\,10^{6}$	0.683

* *p*-value < 0.05 indicates a statistical significance.

offs between sensitivity and specificity, the ROC curve analysis was applied to estimate the overall performance (Figs. 7 and 8). Compared with morphological feature, $GLCM_{ranklet}$ feature had higher area under the ROC curve (AUC) than morphological feature, especially in the identification of TP53 mutation which reaches statistically significant. AUC calculated by the combination of texture and morphological features was similar to individual texture feature.

6. Discussion and conclusion

In this study, the texture and morphology analyses were performed to predict the presence of TP53/PIK3CA mutations, the two most frequent genetic alternations in breast cancer and associated with prognosis and therapeutic response. Many researches showed that TP53 and PIK3CA gene play an important role in cell proliferation, which also occurs angiogenesis and infiltration of surrounding tissues. There were researchers [9–12] extracted texture feature to predict gene mutation. One of these literatures adopted texture and morphological analysis in differencing lower-grade gliomas on brain MRI, and achieved 76.3% accuracy by using first-order statistics, texture, and shape features. To quantify the variability of angiogenesis and infiltration on tumors, texture feature and morphological features were extracted to identify the presence of TP53 and PIK3CA mutations.

The ranklet transform was performed to obtain the horizontal, vertical, and diagonal coefficients before extracting GLCM texture feature. Since the data were collected from multiple institutions, the imaging parameters are different. Texture analysis is influenced by image contrast [44] which mainly defined by repetition time (TR) and spin echo time (TE) of MRI imaging. Therefore, the classification performance of GLCM texture feature with and without ranklet transform was also compared in Tables 7 and 8. The performance of GLCM texture features with ranklet transform ($GLCM_{ranklet}$) was better than GLCM texture feature without ranklet transform ($GLCM_{original}$).

According to the Student's *t*-test used to determine whether each single feature has a significant difference in identifying mutation, TP53 mutated cancers are less textural uniform compared to the cancers

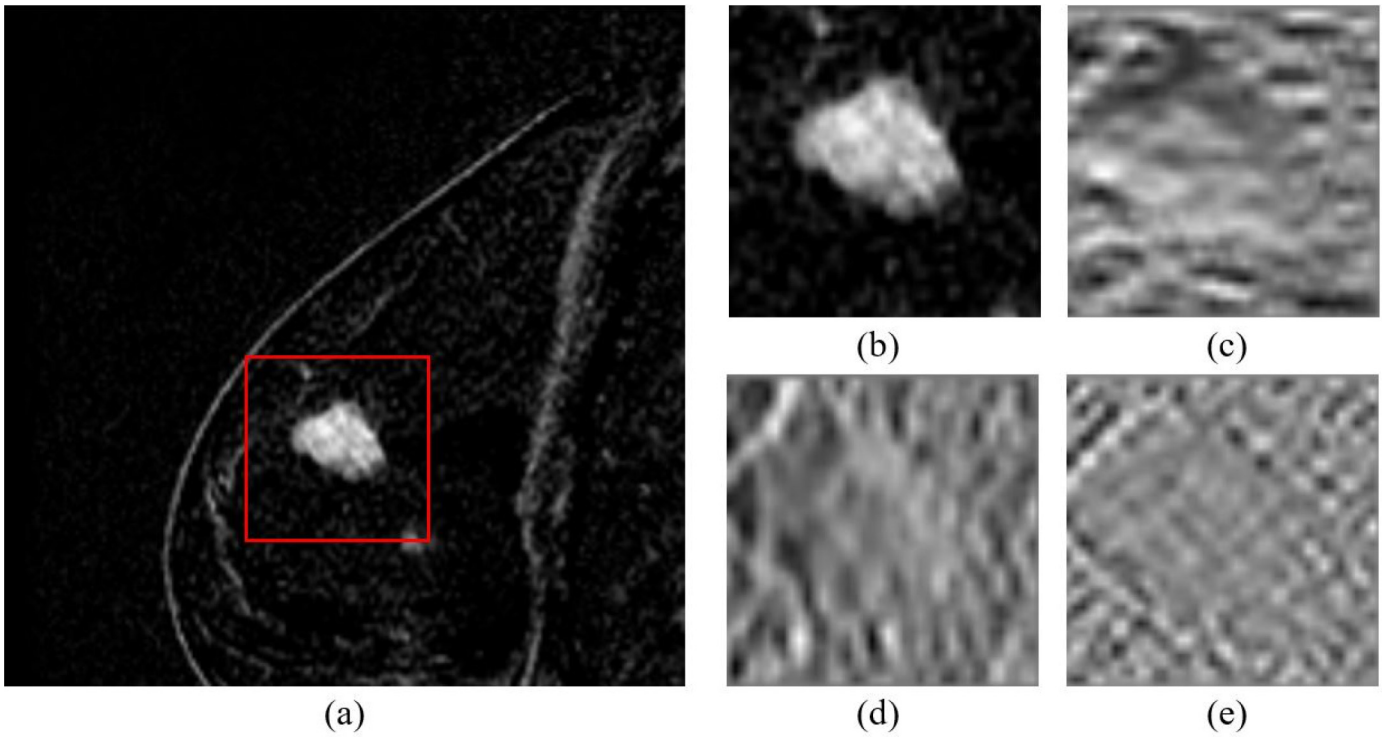

Fig. 5. A cancer case without TP53 mutation. (a) subtraction image; (b) enlarged view of the red frame in (a); (c), (d), and (e) are the ranklet transform results with horizontal, vertical, and diagonal orientations respectively. (For interpretation of the references to colour in this figure legend, the reader is referred to the web version of this article.)

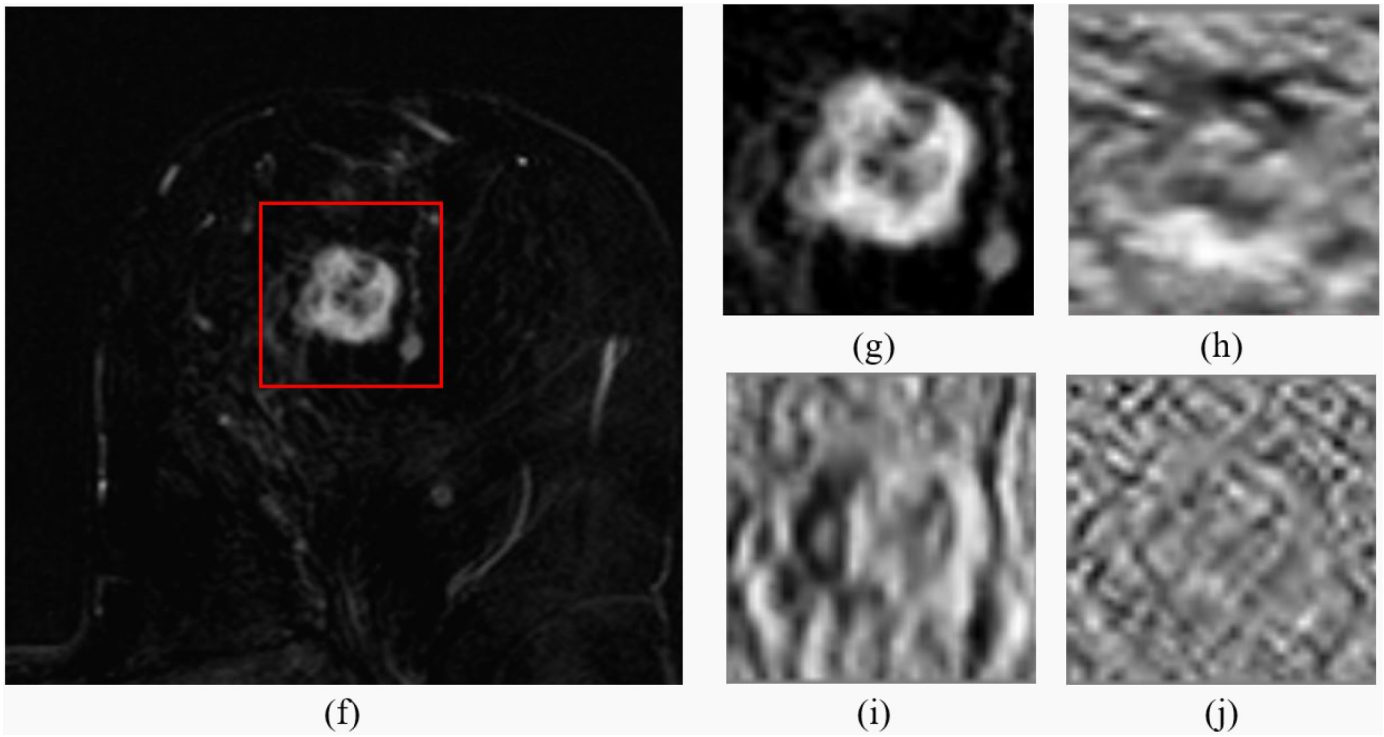

Fig. 6. A cancer case with TP53 mutation. (a) subtraction image; (b) enlarged view of the red frame in (a); (c), (d), and (e) are the ranklet transform results with horizontal, vertical, and diagonal orientations respectively. (For interpretation of the references to colour in this figure legend, the reader is referred to the web version of this article.)

without TP53 mutation (significant higher value of GLCM energy). Pixels in TP53 mutation cancers are more relevant to their neighbors (significant higher value of GLCM correlation). The image contrast of normal TP53 cancers is relatively high (significant higher value of GLCM inertia). In addition, normal TP53 cancers are less variation about intra-tumor intensity (significant higher value of GLCM cluster prominence). In previous studies [45,46], The morphological feature of tumors was outstanding in differentiating between benign tumors and

Table 5
Classification performance of TP53 and PIK3CA mutations by using $GLCM_{ranklet}$ texture feature and morphological feature (dataset A).

	TP53 mutation		PIK3CA mutation	
Feature	$GLCM_{ranklet}$	Morphology	$GLCM_{ranklet}$	Morphology
Accuracy (%)	82.24* (88/107)	64.49 (69/107)	71.03 (76/107)	63.55 (68/107)
Sensitivity (%)	72.50* (29/40)	30.00 (12/40)	74.29 (26/35)	62.86 (22/35)
Specificity (%)	88.06 (59/67)	85.07 (57/67)	69.44 (50/72)	63.89 (46/72)
PPV (%)	78.38 (29/37)	54.55 (12/22)	54.17 (26/48)	45.83 (22/48)
NPV (%)	84.29*(59/70)	67.06 (57/85)	84.75 (50/59)	77.97 (46/59)
AUC	0.78*	0.52	0.70	0.61

* $p < 0.05$ indicates a statistically significant different (chi-square or z-test) between "$GLCM_{ranklet}$" and "Morphology".

Table 6
Classification performance of TP53 mutation by using $GLCM_{ranklet}$ texture feature and morphological feature (dataset B).

	TP53 mutation	
Feature	$GLCM_{ranklet}$	Morphology
Accuracy (%)	76.23 (93/122)	66.39 (81/122)
Sensitivity (%)	72.22 (39/54)	70.37 (38/54)
Specificity (%)	79.41 (54/68)	63.24 (43/68)
PPV (%)	73.58 (39/53)	60.32 (38/63)
NPV (%)	78.26 (54/69)	72.88 (43/59)
AUC	0.81*	0.67

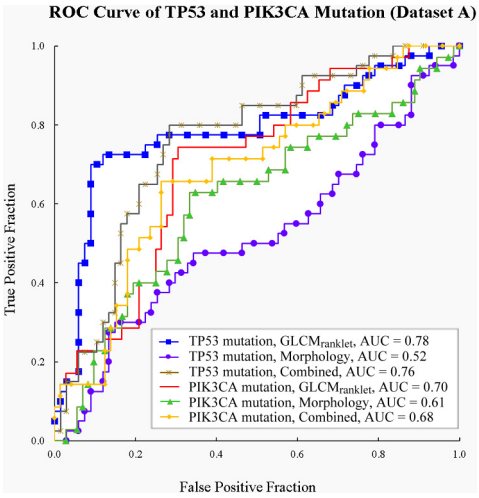

Fig. 7. ROC curves of different feature sets of dataset A.

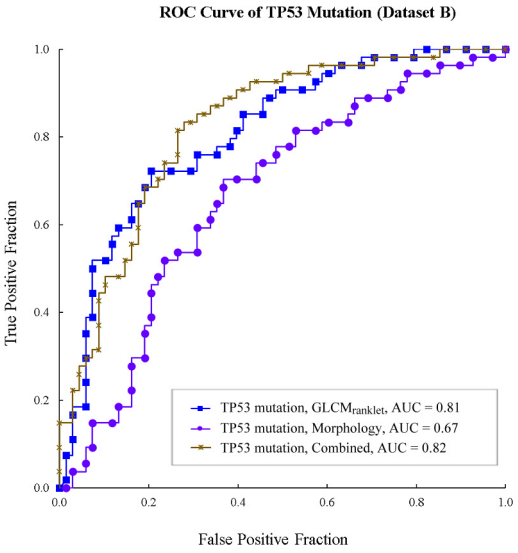

Fig. 8. ROC curves of different feature sets of dataset B.

malignant tumors due to the fact that the growth of benign tumors are usually restricted within a fibrous connective tissue capsule, while malignant tumors are invasive potential and capable of invading adjacent tissues. As the experiment result of this study, the morphological variation between breast cancer with and without TP53/PIK3CA mutation is not obvious enough to identify the presence of TP53/PIK3CA mutations in breast cancer. The reason may be that non-mass lesions were excluded from this study. Morphological features of non-mass enhancement are one of the essential breast MRI characteristics in ACR BI-RADS MRI lexicon [47]. Morphological parameters may be affected by irregularity of the non-mass lesions. Other factors that affect tumor morphology such as background oxygen concentration of tissue [48] where the tumor grows can be further estimated by hypoxic imaging techniques [49] in the future. For overall performance, the classification performance of TP53 mutation in dataset A and dataset B had a certain trend, which reached the similar average performance AUC, and texture feature is significant surpasses to morphological feature.

There are some limitations in this study. First, the semi-automatic tumor segmentation still requires a user-specified seed point and a VOI as the initial of region growing. The region growing method can be combined with tumor detection techniques [50] to define the seed and VOI for fully-automatic segmentation. Second, the data used in this study were collected from different machines. In addition to the different contrast parameters previously mentioned, the DCE-MRI including different number of phases and the interval between phases are greatly variant. In the future, the kinetic curves and different imaging protocol such as T2 weighted image can be considered to investigate the correlation with TP53 mutation using DCE-MRI data that has consistent dynamic parameters.

In conclusion, this study implemented texture and morphological analyses to recognize TP53 mutation and PIK3CA mutation. The GLCM texture feature based on ranklet transform in differentiating the presence of TP53 mutation and PIK3CA mutation achieved higher performance than morphological feature. Quantifying texture feature within breast tumor is potential in recognizing the presence of TP53 mutation and PIK3CA mutation.

Acknowledgments

The authors thank the Ministry of Science and Technology (MOST 107-2634-F-002-013 and MOST 107-2634-F-002-019) for the financial support. This study was also supported by a grant of the Korea Health Technology R&D Project through the Korea Health Industry Development Institute (KHIDI), funded by the Ministry of Health & Welfare, Republic of Korea (HI17C0048). The results published or shown here are in whole or part based upon data generated by the TCGA Research Network: http://cancergenome.nih.gov/.

Table 7
Dataset A classification performance of TP53 and PIK3CA mutation by using GLCM texture feature with ($GLCM_{ranklet}$) and without ranklet transform ($GLCM_{original}$).

	TP53 mutation		PIK3CA mutation	
Feature	$GLCM_{ranklet}$	$GLCM_{original}$	$GLCM_{ranklet}$	$GLCM_{original}$
Accuracy (%)	82.24* (88/107)	67.29 (72/107)	71.03 (76/107)	66.36 (71/107)
Sensitivity (%)	72.50* (29/40)	20.00 (8/40)	74.29 (26/35)	60.00 (21/35)
Specificity (%)	88.06 (59/67)	95.52 (64/67)	69.44 (50/72)	69.44 (50/72)
PPV (%)	78.38 (29/37)	72.73 (8/11)	54.17 (26/48)	48.84 (21/43)
NPV (%)	84.29*(59/70)	66.67 (64/96)	84.75 (50/59)	78.13 (50/64)
AUC	0.78*	0.60	0.70	0.68

* $p < 0.05$ indicates a statistically significant different (chi-square or z-test) between "$GLCM_{ranklet}$" and "$GLCM_{original}$".

Table 8
Dataset B classification performance of TP53 mutation of by using GLCM texture feature with ($GLCM_{ranklet}$) and without ranklet transform ($GLCM_{original}$).

	TP53 mutation	
Feature	$GLCM_{ranklet}$	$GLCM_{original}$
Accuracy (%)	76.23 (93/122)	72.13 (88/122)
Sensitivity (%)	72.22 (39/54)	75.93 (41/54)
Specificity (%)	79.41 (54/68)	69.12 (47/68)
PPV (%)	73.58 (39/53)	66.13 (41/62)
NPV (%)	78.26 (54/69)	78.33 (47/60)
AUC	0.81	0.75

Appendix A. Supplementary data

Supplementary data to this article can be found online at https://doi.org/10.1016/j.mri.2019.08.026.

References

[1] Levine AJ, Oren M. The first 30 years of p53: growing ever more complex. Nat Rev Cancer 2009;9:749–58. https://doi.org/10.1038/nrc2723.
[2] Williams AB, Schumacher B. p53 in the DNA-damage-repair process. Cold Spring Harb Perspect Med 2016;6. https://doi.org/10.1101/cshperspect.a026070.
[3] Atha DH, Wenz HM, Morehead H, Tian J, O'Connell CD. Detection of p53 point mutations by single strand conformation polymorphism: analysis by capillary electrophoresis. Electrophoresis 1998;19:172–9. https://doi.org/10.1002/elps.1150190207.
[4] Keller G, Hartmann A, Mueller J, Hofler H. Denaturing high pressure liquid chromatography (DHPLC) for the analysis of somatic p53 mutations. Lab Invest 2001;81:1735–7.
[5] Ruppert JM, Stillman B. Analysis of a protein-binding domain of P53. Mol Cell Biol 1993;13:3811–20. [doi].
[6] Baas IO, Mulder JW, Offerhaus GJ, Vogelstein B, Hamilton SR. An evaluation of six antibodies for immunohistochemistry of mutant p53 gene product in archival colorectal neoplasms. Journal of Pathology 1994;172:5–12. https://doi.org/10.1002/path.1711720104.
[7] Levesque MA, Yu H, Clark GM, Diamandis EP. Enzyme-linked immunoabsorbent assay-detected p53 protein accumulation: a prognostic factor in a large breast cancer cohort. J Clin Oncol 1998;16:2641–50. [doi].
[8] Puhalla H, Kandioler D, Ludwig C, Filipits M, Wrba F, Laengle F, et al. P53 analysis in gallbladder cancer: comparison of gene analysis versus immunohistochemistry. Anticancer Res 2004;24:1201–6. [doi].
[9] Dang M, Lysack JT, Wu T, Matthews TW, Chandarana SP, Brockton NT, et al. MRI texture analysis predicts p53 status in head and neck squamous cell carcinoma. Am J Neuroradiol 2015;36:166–70. https://doi.org/10.3174/ajnr.A4110.
[10] Moon WK, Shen YW, Huang CS, Chiang LR, Chang RF. Computer-aided diagnosis for the classification of breast masses in automated whole breast ultrasound images. Ultrasound in Medicine and Biology 2011;37:539–48. https://doi.org/10.1016/j.ultrasmedbio.2011.01.006.
[11] Weiss GJ, Ganeshan B, Miles KA, Campbell DA, Cheung PY, Frank S, et al. Noninvasive image texture analysis differentiates K-ras mutation from pan-wildtype NSCLC and is prognostic. Clin Cancer Res 2014;20. https://doi.org/10.1158/1078-0432.14AACRIASLC-A34.
[12] Teo ZL, Provenzano E, Dite GS, Park DJ, Apicella C, Sawyer SD, et al. Tumour morphology predicts PALB2 germline mutation status. Br J Cancer 2013;109:154–63. https://doi.org/10.1038/bjc.2013.295.
[13] Krizmanich-Conniff KM, Paramagul C, Patterson SK, Helvie MA, Roubidoux MA, Myles JD, et al. Triple receptor-negative breast cancer: imaging and clinical characteristics. Am J Roentgenol 2012;199:458–64. https://doi.org/10.2214/Ajr.10.6096.
[14] Li B, Zhao X, Dai SC, Cheng W. Associations between mammography and ultrasound imaging features and molecular characteristics of triple-negative breast cancer. Asian Pac J Cancer Prev 2014;15:3555–9. https://doi.org/10.7314/Apjcp.2014.15.8.3555.
[15] Yu YF, Zhang Y, Shen N, Zhang RY, Lu XQ. Effect of VEGF, P53 and telomerase on angiogenesis of gastric carcinoma tissue. Asian Pac J Trop Med 2014;7:293–6. https://doi.org/10.1016/S1995-7645(14)60041-9.
[16] Soler A, Serra H, Pearce W, Angulo A, Guillermet-Guibert J, Friedman LS, et al. Inhibition of the p110 alpha isoform of PI 3-kinase stimulates nonfunctional tumor angiogenesis. Journal of Experimental Medicine 2013;210:1937–45. https://doi.org/10.1084/jem.20121571.
[17] Chang RF, Chen HH, Chang YC, Huang CS, Chen JH, Lo CM. Quantification of breast tumor heterogeneity for ER status, HER2 status, and TN molecular subtype evaluation on DCE-MRI. Magn Reson Imaging 2016;34:809–19. https://doi.org/10.1016/j.mri.2016.03.001.
[18] Davnall F, Yip CS, Ljungqvist G, Selmi M, Ng F, Sanghera B, et al. Assessment of tumor heterogeneity: an emerging imaging tool for clinical practice? Insights Imaging 2012;3:573–89. https://doi.org/10.1007/s13244-012-0196-6.
[19] Haralick RM, Shanmugam K, Dinstein I. Textural features for image classification. Ieee Transactions on Systems Man and Cybernetics 1973(Smc3):610–21. https://doi.org/10.1109/Tsmc.1973.4309314.
[20] Masotti M, Campanini R. Texture classification using invariant ranklet features. Pattern Recognition Letters 2008;29:1980–6. https://doi.org/10.1016/j.patrec.2008.06.01.
[21] Meinel LA, Stolpen AH, Berbaum KS, Fajardo LL, Reinhardt JM. Breast MRI lesion classification: improved performance of human readers with a backpropagation neural network computer-aided diagnosis (CAD) system. J Magn Reson Imaging 2007;25:89–95. https://doi.org/10.1002/jmri.20794.
[22] Bribiesca E. An easy measure of compactness for 2D and 3D shapes. Pattern Recognition 2008;41:543–54. https://doi.org/10.1016/j.patcog.2007.06.029.
[23] Mulchrone KF, Choudhury KR. Fitting an ellipse to an arbitrary shape: implications for strain analysis. Journal of Structural Geology 2004;26:143–53. https://doi.org/10.1016/S0191-8141(03)00093-2.
[24] Zhu Q, L-K P. A transformation-invariant recursive subdivision method for shape analysis. Presented at the 9th international conference on pattern recognition. 1988.
[25] Clark K, Vendt B, Smith K, Freymann J, Kirby J, Koppel P, et al. The cancer imaging archive (TCIA): maintaining and operating a public information repository. J Digit Imaging 2013;26:1045–57. https://doi.org/10.1007/s10278-013-9622-7.
[26] Lingle W, Erickson BJ, Zuley ML, Jarosz R, Bonaccio E, Filippini J, et al. Radiology data from the cancer genome atlas breast invasive carcinoma [TCGA-BRCA] collection. The Cancer Imaging Archive 2016. https://doi.org/10.7937/K9/TCIA.2016.AB2NAZRP.
[27] Hojjatoleslami SA, Kittler J. Region growing: a new approach. IEEE Trans Image Process 1998;7:1079–84. https://doi.org/10.1109/83.701170.
[28] Field AP. Discovering statistics using SPSS: (and sex, drugs and rock "n" roll). *3rd ed.* Los Angeles: SAGE Publications; 2005.
[29] Nishida N, Yano H, Nishida T, Kamura T, Kojiro M. Angiogenesis in cancer. Vasc Health Risk Manag 2006;2:213–9. [doi].
[30] Rosen BR, Belliveau JW, Vevea JM, Brady TJ. Perfusion imaging with NMR contrast agents. Magn Reson Med 1990;14:249–65.
[31] Whitaker R, Xue X. Variable-conductance, level-set curvature for image denosing presented at the IEEE international conference on image processing2001.
[32] Piekos T. Confidence connected segmentation using ITK. The Insight Journal 2007. [doi] http://hdl.handle.net/1926/1306.
[33] Iba'nez L, Schroeder W, Ng L, Cates J, and Consortium tIS, The ITK software guide., 2 ed., 2005.
[34] Schad LR. Problems in texture analysis with magnetic resonance imaging. Dialogues Clin Neurosci 2004;6:235–42.
[35] Lim JS. Two-dimensional signal and image processing. New Jersey: Prentice Hall; 1990.
[36] Poynton CA. Gamma and its disguises - the nonlinear mappings of intensity in perception, Crts, film, and video. Smpte Journal 1993;102:1099–108. [doi].
[37] Chen W, Giger ML, Li H, Bick U, Newstead GM. Volumetric texture analysis of breast lesions on contrast-enhanced magnetic resonance images. Magn Reson Med 2007;58:562–71. https://doi.org/10.1002/mrm.21347.
[38] Karahaliou A, Vassiou K, Arikidis NS, Skiadopoulos S, Kanavou T, Costaridou L. Assessing heterogeneity of lesion enhancement kinetics in dynamic contrast-enhanced MRI for breast cancer diagnosis. Br J Radiol 2010;83:296–309. https://doi.

org/10.1259/bjr/50743919.
[39] Sutton EJ, Dashevsky BZ, Oh JH, Veeraraghavan H, Apte AP, Thakur SB, et al. Breast Cancer molecular subtype classifier that incorporates MRI features. J Magn Reson Imaging 2016;44:122–9. https://doi.org/10.1002/jmri.25119.
[40] Wang TC, Huang YH, Huang CS, Chen JH, Huang GY, Chang YC, et al. Computer-aided diagnosis of breast DCE-MRI using pharmacokinetic model and 3-D morphology analysis. Magn Reson Imaging 2014;32:197–205. https://doi.org/10.1016/j.mri.2013.12.002.
[41] Kohavi R, John GH. Wrappers for feature subset selection. Artificial Intelligence 1997;97:273–324. https://doi.org/10.1016/S0004-3702(97)00043-X.
[42] Xiao Y, Hua J, Dougherty ER. Quantification of the impact of feature selection on the variance of cross-validation error estimation. EURASIP J Bioinform Syst Biol 2007. https://doi.org/10.1155/2007/16354. 16354.
[43] Holm S. A simple sequentially Rejective multiple test procedure. Scand J Stat 1979;6:65–70.
[44] Yang MC, Moon WK, Wang YCF, Bae MS, Huang CS, Chen JH, et al. Robust texture analysis using multi-resolution gray-scale invariant features for breast sonographic tumor diagnosis. IEEE Trans Med Imaging 2013;32:2262–73. https://doi.org/10.1109/Tmi.2013.2279938.
[45] Huang YH, Chang YC, Huang CS, Wu TJ, Chen JH, Chang RF. Computer-aided diagnosis of mass-like lesion in breast MRI: differential analysis of the 3-D morphology between benign and malignant tumors. Comput Methods Programs Biomed 2013;112:508–17. https://doi.org/10.1016/j.cmpb.2013.08.016.
[46] Sirica AE. The pathobiology of neoplasia. New York: Plenum Press; 1989.
[47] Wenkel E, Heckmann M, Heinrich M, Schwab SA, Uder M, Schulz-Wendtland R, et al. Automated breast ultrasound: lesion detection and BI-RADS (TM) classification - a pilot study. Rofo-Fortschritte Auf Dem Gebiet Der Rontgenstrahlen Und Der Bildgebenden Verfahren 2008;180:804–8. https://doi.org/10.1055/s-2008-1027563.
[48] Gerlee P, Anderson ARA. Diffusion-limited tumour growth: simulations and analysis. Math Biosci Eng 2010;7:385–400. https://doi.org/10.3934/mbe.2010.7.385.
[49] Gaertner FC, Souvatzoglou M, Brix G, Beer AJ. Imaging of hypoxia using PET and MRI. Curr Pharm Biotechnol 2012;13:552–70. [doi].
[50] Chang YC, Huang YH, Huang CS, Chen JH, Chang RF. Computerized breast lesions detection using kinetic and morphologic analysis for dynamic contrast-enhanced MRI. Magn Reson Imaging 2014;32:514–22. https://doi.org/10.1016/j.mri.2014.01.008.